

Whitlow W.L. Au
Arthur N. Popper
Richard R. Fay
Editors

Hearing by Whales and Dolphins

With 152 Illustrations



Springer

10

Acoustic Models of Sound Production and Propagation

JAMES L. AROYAN, MARK A. McDONALD, SPAIN C. WEBB,
JOHN A. HILDEBRAND, DAVID CLARK, JEFFREY T. LAITMAN, and
JOY S. REIDENBERG

1. Introduction

Acoustic models based on physics and mathematics may yield significant advances in the understanding of sound production, propagation, and interaction associated with whales and dolphins. Models can be used to estimate the limits of intensity and frequency that are physically possible given the anatomy of a species. Models can also tell us what kind of anatomical structures would be necessary in order to produce sound having specific characteristics. Models can be used to clarify what type of measurements should be performed to answer specific questions. Many areas of bioacoustics stand to benefit from simulation of sound propagation through biological tissues and the media surrounding them. However, accurate modeling of biological subjects with complex anatomical features is extremely challenging, and few modern studies exist of sound production and propagation in whales and dolphins.

In this chapter, we will consider two acoustic models, the first dealing with the propagation of echolocation signals through the head of a dolphin. This model combines a novel tissue modeling approach with techniques of numerical wave propagation to study the acoustic principles operating in the biosonar emission and reception processes. The second model deals with the production of low-frequency sounds by the blue whale, *Balaenoptera musculus*. The features of blue whale sounds are considered and a sound production mechanism is derived taking the structures of the whale's anatomy into account along with the physics of acoustics. The first model results from the research of Aroyan (1996) and the second model is the result of research by the remaining authors.

2. Three-Dimensional Numerical Simulation of Biosonar Emission in the Common Dolphin

Measurements of the acoustic field of echolocating dolphins have demonstrated that dolphins emit a rapid series of intense pulses in a narrowly focused beam that emanates from the forehead and rostrum. Despite application of a variety of experimental techniques, the exact mechanisms involved in the generation, emission, and reception of delphinid biosonar signals have remained conjectural. Advances in the methodology of bioacoustic simulations have led to powerful combinations of techniques capable of addressing questions that have proven difficult to resolve experimentally. Aroyan (1996) combined methods for three-dimensional (3-D) acoustic simulation and far-field extrapolation with a novel approach to the mapping of acoustic tissue parameters from X-ray computed tomographic (CT) data. These techniques, applied to models of the forehead and lower jaw tissues of the common dolphin, *Delphinus delphis*, enabled a detailed study of the patterns of sound propagation within the modeled tissues and, hence, of the acoustic principles operating in the biosonar emission and reception processes. The following sections discuss the methods used in this investigation and present a series of results concerning the location of the biosonar signal source tissues, the roles of the skull, air sacs, and soft tissues (including the melon) in beam formation, and the acoustical consequences of forehead asymmetry in *Delphinus delphis*.

2.1 Computational Methods

The following approach was used to investigate the *D. delphis* emission system. First, computer models of the tissues of the dolphin's head were constructed using a novel mapping of both tissue density and acoustic velocity from X-ray CT attenuation data to a simulation grid. Second, 3-D finite difference programs were used to simulate acoustic propagation into the tissue models to locate the source region of the dolphin's biosonar emissions (analogous to the use of inverse seismologic simulations to pinpoint the underground source point or "hypocenter" of an earthquake, or to reversing the emission/collection role of an optical lens system). Third, sources were placed at these inverse simulation "hypocenters" or at conjectured anatomical source locations, and finite difference programs were again used to propagate the acoustic field of the source and tissue models out to a surface surrounding the tissue region of the grid. Fourth, boundary extrapolation programs were used to compute the emitted acoustic far-field from the pressure and its normal derivative over this surface. Biosonar mechanisms were investigated by visualizing the acoustic energy density within a variety of tissue models and by comparing the fields emitted by these models to the experimentally measured sonar emissions of live animals. Conceptually, this approach involves: (1) constructing the best pos-

sible acoustical model of the dolphin's tissues from the available data; (2) utilizing the reversibility of wave propagation to let the model tell us what its focal characteristics are; and (3) applying the resulting focal information in forward simulations to determine the emission properties for each model. Each step of this procedure has yielded new insights into the acoustic mechanisms of delphinid biosonar.

In order to study the patterns of sound propagation within the forehead tissues, propagation through tissue models was simulated by numerical integration of the acoustic wave equation. Shear wave velocities for soft tissues remain less than 1% of the compressional wave sound speed for frequencies below 1 MHz, and soft tissue shear wave attenuation coefficients are of the order of 10^4 times the compressional wave attenuation coefficients (Frizzell et al., 1976; Carstensen 1979; Madsen, et al., 1983). Additionally, the fact that air sacs normally cover much of the skull surface in the vicinity of the nasal passages in delphinids also suggests that shear modes do not play a significant role in biosonar emissions. In the current simulations, tissues (including bone) were modeled as inhomogeneous fluids and shear wave modes were ignored.

In fluids of inhomogeneous density and velocity, the linearized wave equation for acoustic pressure p is (Pierce 1981; Aroyan 1990):

$$\frac{1}{c^2(\mathbf{x})} \frac{\partial^2 p}{\partial t^2} = \nabla^2 p - \frac{\nabla p \cdot \nabla \rho(\mathbf{x})}{\rho(\mathbf{x})} \quad (1a)$$

Both the sound speed c and density ρ are functions of position \mathbf{x} , while the acoustic pressure p is dependent on position and time, $p = p(\mathbf{x}, t)$. By mapping the values of tissue velocity and density onto a grid, finite differencing schemes can be used to propagate the solution of Eq. 1a forward in time. The following discretization of Eq. 1a, solved for the numerical value of the acoustic pressure $P_{i,j,k}^{m+1}$ at grid position (i, j, k) and time step $(m + 1)$, was applied over the tissue region of the grid:

$$\begin{aligned} P_{i,j,k}^{m+1} = & (2 - 7.5\kappa_{i,j,k}^2)P_{i,j,k}^m - P_{i,j,k}^{m-1} \\ & + \frac{4\kappa_{i,j,k}^2}{3} [P_{i+1,j,k}^m + P_{i-1,j,k}^m + P_{i,j+1,k}^m + P_{i,j-1,k}^m + P_{i,j,k+1}^m + P_{i,j,k-1}^m] \\ & - \frac{\kappa_{i,j,k}^2}{12} [P_{i+2,j,k}^m + P_{i-2,j,k}^m + P_{i,j+2,k}^m + P_{i,j-2,k}^m + P_{i,j,k+2}^m + P_{i,j,k-2}^m] \\ & - \frac{\kappa_{i,j,k}^2}{3\rho_{i,j,k}} [(P_{i+1,j,k}^m - P_{i-1,j,k}^m) - (P_{i+2,j,k}^m + P_{i-2,j,k}^m)/8](\rho_{i+1,j,k} - \rho_{i-1,j,k}) \\ & - \frac{\kappa_{i,j,k}^2}{3\rho_{i,j,k}} [(P_{i,j+1,k}^m - P_{i,j-1,k}^m) - (P_{i,j+2,k}^m + P_{i,j-2,k}^m)/8](\rho_{i,j+1,k} - \rho_{i,j-1,k}) \\ & - \frac{\kappa_{i,j,k}^2}{3\rho_{i,j,k}} [(P_{i,j,k+1}^m - P_{i,j,k-1}^m) - (P_{i,j,k+2}^m + P_{i,j,k-2}^m)/8](\rho_{i,j,k+1} - \rho_{i,j,k-1}) \quad (1b) \end{aligned}$$

In this equation, $\kappa_{i,j,k} = (l/h)c_{i,j,k}$ is a nondimensionalized version of the spatially varying acoustic velocity $c_{i,j,k}$; $\rho_{i,j,k}$ is the spatially varying density; and $l = \Delta t$ and $h = \Delta x = \Delta y = \Delta z$ are the temporal and spatial grid increments, respectively. This scheme is fourth order in the spatial derivatives of pressure, second order in the spatial derivatives of density, and second order in the time derivative of pressure. The first three lines of Eq. 1b constitute the scheme for the homogeneous wave equation. This homogeneous scheme was used outside the tissue regions of the grid and greater than two points away from the grid edges. A second order spatial derivative scheme was applied at the next-to-last grid points. Absorbing boundary conditions were applied at the extreme grid edges to reduce reflections from grid boundaries to very low levels.

Figure 10.1a illustrates a typical simulation grid layout. The region of the grid containing the tissue model is indicated. Except for a few trials on half-resolution grids, a 1.5-mm cubic grid corresponding to the finest X-ray CT data voxel size was used in the forehead simulations. For the inverse simulations, the front face of the grid was used as a flat source to ensonify the tissue model region with a cosine-windowed "echo" at a fixed frequency and angle of return. A windowed aperture function was used to reduce the near-field diffraction of this source. The energy density at the focal maxima found in the inverse simulations were two to three orders of magnitude above variations caused by near-field diffraction and uneven ensonification of the model region.

Several different quantities may be calculated from the simulated pressure field and visualized with graphics packages in order to illustrate the patterns of sound propagation within the tissue models. For example, one may visualize the time-averaged magnitude of the total acoustic energy density W_{total} as the sum of the potential acoustic energy density $W_{potential}$ and the kinetic acoustic energy density $W_{kinetic}$ (Pierce 1981; Morse and Ingard 1968)

$$W_{total} = W_{potential} + W_{kinetic} = \frac{1}{2\rho c^2} [\text{Re}(p)]^2 + \frac{\rho}{2} |\text{Re}(\mathbf{u})|^2 \quad (2)$$

where the vector fluid velocity $\mathbf{u} = \nabla p / (i\omega\rho)$. Alternatively, one may visualize the time-averaged magnitude of the potential energy density $W_{potential} = [\text{Re}(p)]^2 / (2\rho c^2)$, as in Aroyan (1996). In this chapter, we will visualize either the total or the potential acoustic energy density, although all three forms of energy density (potential, kinetic, or total) and/or the acoustic intensity vector yield significant information regarding propagation within tissues.

In order to compute the emitted far-field patterns of various source and tissue models, the simulated pressure field and its normal derivative over a rectangular surface immediately surrounding the tissue region of the grid was used as input to boundary integral extrapolation programs. The

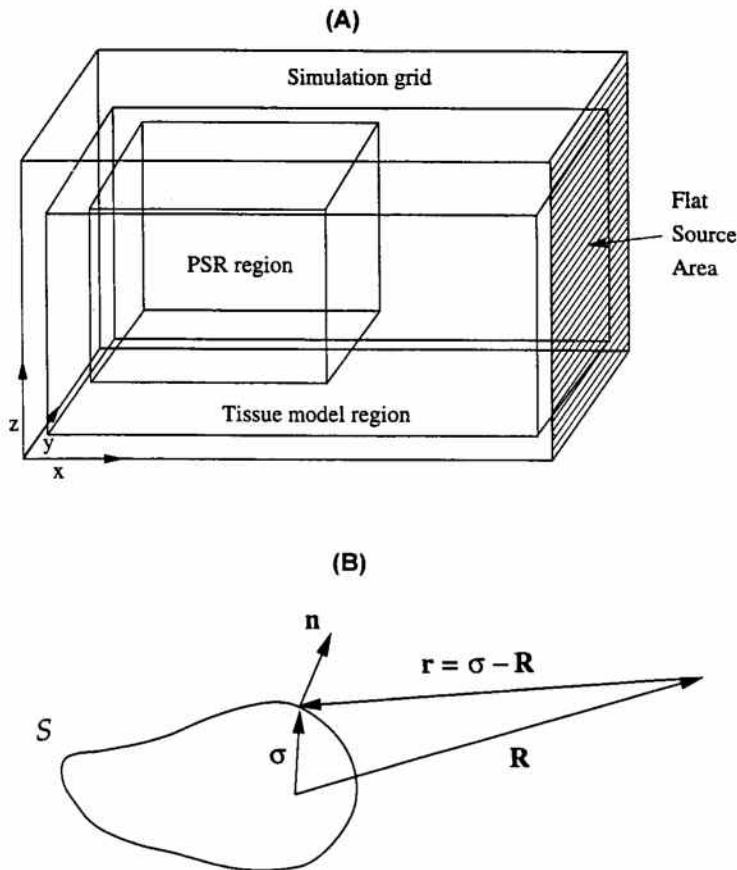


FIGURE 10.1. (A) Typical simulation grid layout. All inverse simulations used the front face of the grid as a flat source to ensound the tissue region with “echoes” at various angles of return. In the inverse forehead simulations, the acoustic energy density within the subvolume labeled “PSR” was visualized. In all forward simulations, the pressure and its normal derivative over a surface immediately surrounding the source and tissue model were used to compute the far-field emission patterns. (B) Diagram of the geometry assumed by Eq. 3. Field points \mathbf{R} are assumed to lie in the sourceless and homogeneous region exterior to the extrapolation surface S , which encloses an arbitrary source volume.

Helmholtz integral equation relates the pressure p and the normal derivative of the pressure $\partial p/\partial n$ over a surface S surrounding an arbitrary distribution of sources to the pressure $p(\mathbf{R})$ produced by those sources at any field point \mathbf{R} (Baker and Copson 1953; Copley 1968; Schenck 1968). The geometry assumed here is illustrated in Figure 10.1b. For

points \mathbf{R} lying exterior to the source volume enclosed by surface S , the Helmholtz integral equation has the form (Junger and Feit 1986; Aroyan 1996)

$$p(\mathbf{R}) = -\oint_S \left\{ p(\boldsymbol{\sigma}) \frac{\partial G(\boldsymbol{\sigma}, \mathbf{R})}{\partial n} - G(\boldsymbol{\sigma}, \mathbf{R}) \frac{\partial p(\boldsymbol{\sigma})}{\partial n} \right\} dS(\boldsymbol{\sigma}) \quad (3)$$

Here $\boldsymbol{\sigma}$ defines the vector coordinates of surface S , while $\partial/\partial n = \mathbf{n} \cdot \nabla$ denotes the directional derivative along the outward pointing unit vector \mathbf{n} normal to surface S . We have also used the notation $G(\boldsymbol{\sigma}, \mathbf{R})$ for the 3-D free-space Green's function,

$$G(\boldsymbol{\sigma}, \mathbf{R}) = -\frac{e^{ik|\boldsymbol{\sigma}-\mathbf{R}|}}{4\pi|\boldsymbol{\sigma}-\mathbf{R}|} = -\frac{e^{ikr}}{4\pi r}, \quad \mathbf{r} = \boldsymbol{\sigma} - \mathbf{R}, \quad (4)$$

where $k = \omega/c$ is the acoustic wave number, ω is the angular frequency of the field, and c is the (constant) speed of sound propagation at surface S and in the medium external to S . No assumptions are made about the distribution of sound sources, speeds, or other properties of materials inside surface S —this source region may be arbitrarily complex. In addition, S may be any closed surface surrounding the source region. The medium external to S , however, is assumed to be infinite, homogeneous, and sourceless. Because the extrapolation surface S can be located immediately outside the tissue model region of the simulation grid, an enormous reduction of the grid size required for far-field calculation is realized. In the current bioacoustic application, a far-field form of Eq. 3 was utilized: Appendix A gives this far-field formulation and notes aspects of its numerical implementation. Appendix A also provides an example of a simple computed far-field pattern and introduces an efficient representation of this data over all emission directions, which is used in all emission diagrams of Section 3.

2.2 Model of the Dolphin

This section outlines a new approach to modeling the acoustic parameters of delphinid soft tissues from X-ray CT attenuation data. This method generates approximations of the 3-D density and velocity distributions within scanned delphinid tissues that agree well with reported measurements.

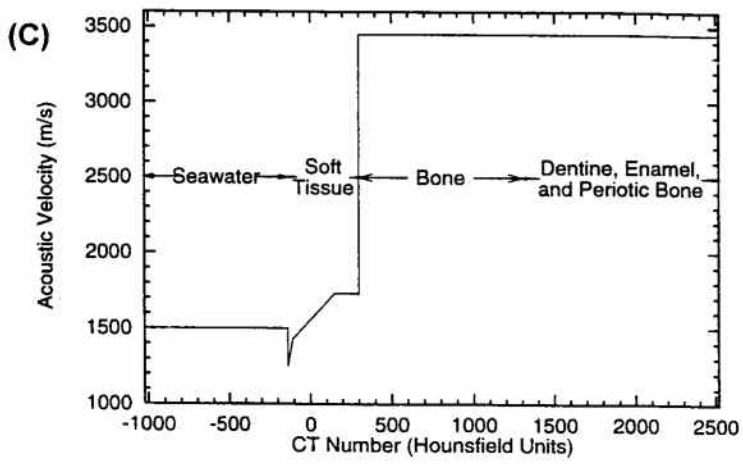
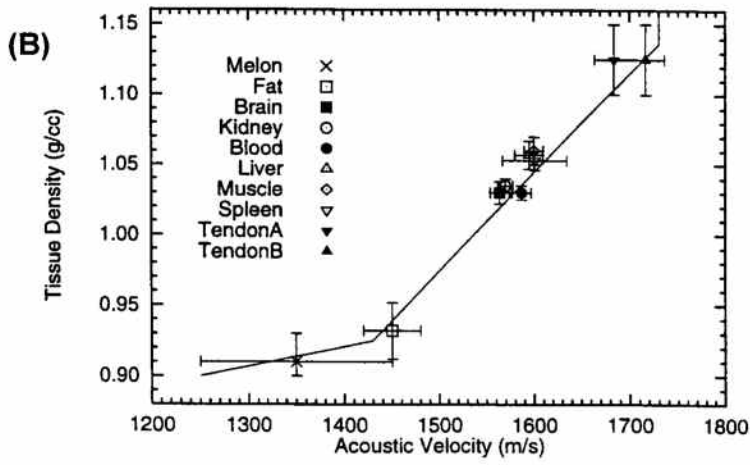
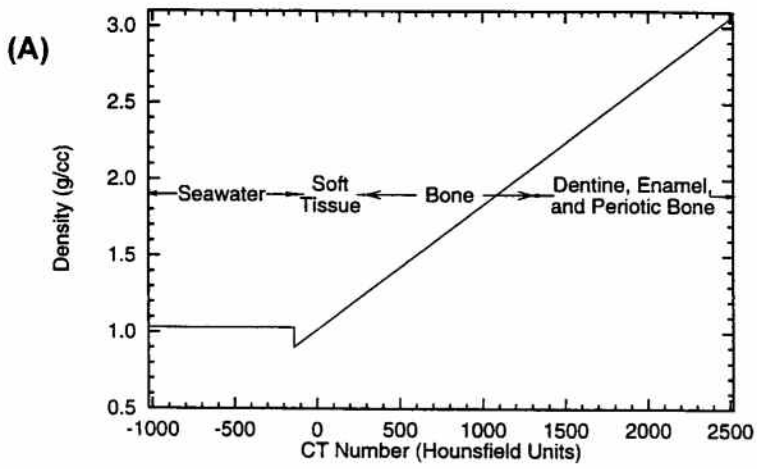
An X-ray CT scan of the head of a male (body length = 1.92 m) common dolphin, *D. delphis*, was provided by Dr. Ted W. Cranford (identified as specimen D4 in Cranford et al. 1996). The spacing of the scan planes in the original CT data set varied from 5.0 mm over the rostrum, to 1.5 mm over the narial region, to 3.0 mm over the posterior cranium. Individual scans consisted of 320×320 pixel transverse sectional images on a 1.5-mm square grid. For simulation purposes, the tissue region of the original data was linearly interpolated in the x-direction to planes uniformly spaced 1.5 mm apart. The resulting data set was then used either at full resolution

(on a 1.5-mm cubic grid) or half resolution (on a 3.0-mm cubic grid).

For the GE CT9800 scanner used to collect the *D. delphis* data, a linear mapping between X-ray attenuation values in Hounsfield Units (HU) and human tissue density has been shown to be accurate to within $\pm 5\%$ for densities ranging from soft tissue to cortical bone (Henson, Ackland, and Fox 1987). The slope of this correspondence varies with the beam energy of the scanner. Application of more precise medical techniques for tissue HU-to-density mapping could potentially reduce these errors to well below 1% (Erlichman 1986; Cann 1988; Hunter 1988). The present study assumed that the scan image pixel values were linearly related to Hounsfield Units, and mapped tissue densities from HU values using the linear model shown in Figure 10.2a. Three calibration points confirming this map were provided by the known density (0.90 g/cc) of the inner melon (Varanasi et al. 1975), the known density (1.18 g/cc) of the plexiglass specimen registration frame, and the maximum density (roughly 2.7 g/cc) of delphinid periotic bone (Lees et al. 1996). The image scale ranges from -1,024 to +2,519 HU. The low end of the scale (below -138 HU) was below all soft tissue structures (except air sacs, which were handled separately). Since it was necessary to map the air surrounding the scanned specimen to seawater, this lower range is mapped to the density of seawater (1.03 g/cc) in Figure 10.2a.

Tissue velocity was then deduced from the above tissue density information and the following experimental data. Figure 10.2b plots average experimental density and velocity values and approximate ranges for several types of normal (fresh) terrestrial mammalian soft tissues and delphinid melon lipids at 37°C from literature sources. Terrestrial mammalian tissue data was taken from Parry and Chivers (1979), Goss et al. (1980), Lele and Sleefe (1985), and Miles (1996). Bottlenose dolphin melon lipid velocity data was taken primarily from Norris and Harvey (1974) and secondarily from Litchfield et al. (1979), since the latter study measured the velocities of lipid samples after extraction from melon and blubber tissues. Extraction of the lipids from connective tissue components probably lowered the values reported for the velocities of the "outer" and "under" melon. Both papers agree approximately on the velocity range for the inner melon tissues. Melon and lower jaw lipid densities (down to .90 g/cc) are taken from Varanasi, Feldman, and Malins (1975) assuming a 60% to 40% by weight triglyceride-isovalerate wax ester melon lipid composition, which is similar across the family Delphinidae (Litchfield et al. 1975). Although few measurements of intact tissue velocity, density, and temperature are available, an attempt was made to define the ranges for the normal mammalian tissues in Figure 10.2b as 1-sigma deviations in the tabulated values. The density and velocity ranges for delphinid melon lipids shown in Figure 10.2b correspond to the ranges that exist within the layered melon tissues.

It is important to note that the velocity of terrestrial mammalian soft tissues is correlated approximately linearly with density in the range from



normal fat to tendon. The lipids of the delphinid melon and lower jaw are, however, chemically and acoustically distinct from other body fats and blubber (Litchfield et al. 1973; Litchfield et al. 1975, 1979; Malins and Varanasi 1975; Varanasi et al. 1975; Varanasi et al. 1982). It therefore makes sense to correlate the velocities of all soft tissues except the melon and lower jaw fats with their densities using a linear mapping from ordinary fat to tendon for the characteristic mammalian soft tissue range. The unique "acoustic fats" can then be incorporated by adding an extension from normal fat down to the lower melon lipid density and velocity threshold. Given the magnitude of the variations in mammalian soft tissue densities and velocities, a two part linear mapping was deemed satisfactory for the series of simulations reported here. The acoustic phenomena of interest to this study result mainly from relatively short propagation paths (10 wavelengths or less) through dermal layers, blubber, melon fat, muscle, and connective tissues. Because biologically reasonable variation of the velocity mapping did not produce significantly different results, the velocities of these tissues was presumed to be adequately represented by the current model. This piecewise linear mapping of density versus velocity for the soft tissue range is indicated by the solid line in Figure 10.2b, demonstrating that a good correspondence can be achieved between soft tissue velocity and density. The current study is the first to have approximated the 3-D density and velocity structures of all soft tissues including the melon and lower jaw fats and to have accurately simulated 3-D acoustic propagation within those structures. Diagrams of the resulting tissue density, velocity, and impedance structure in a right parasagittal section through the core of the *D. delphis* melon can be found in Aroyan (1996). Previous analytical and ray tracing studies had assumed highly simplified two-dimensional tissue density and/or velocity models. (Compare, for example, Evans et al. 1964; Dubrovskiy and Zaslavskiy 1975; Litchfield et al. 1979; Aroyan et al. 1992; Au 1993).

Because the HU-to-density map has already been specified (Figure 10.2a), the empirical density-to-velocity map (Figure 10.2b) then determines the soft tissue HU-to-velocity mapping. The HU-to-velocity mapping

←

FIGURE 10.2. (A) Plot of the linear mapping from CT values (in Hounsfield Units) to tissue density used in the simulations. Tissue types corresponding to mapped CT ranges have been indicated. (B) Plot of approximate values and ranges of density and velocity for several types of normal terrestrial mammalian soft tissues and delphinid melon lipids measured at 37°C. Tendon A refers to propagation perpendicular to the tendon fiber bundles. Tendon B refers to propagation along the tendon fiber axis. The solid line indicates the piecewise linear mapping of density to velocity used in the simulations over the range of soft tissues. (C) Plot of the mapping from CT values (in Hounsfield Units) to tissue velocity used in the simulations. This mapping (over the soft tissue range) is implied by the upper two figures. Tissue types corresponding to mapped CT ranges have been indicated.

used in this study is pictured in Figure 10.2c. The soft tissue range of this mapping generates good agreement between Cranford's (1992) plots of HU values through a *Tursiops truncatus* melon and Norris and Harvey's (1974) *T. truncatus* melon velocity measurements. While intact tissue velocities for *D. delphis* have not been measured, it is reasonable to expect that a mapping based on the measured acoustic properties of mammalian tissues and that appears to work for *T. truncatus* will work for other delphinids as well, provided the data ranges for each specimen have been properly determined. Similar triglyceride and isovalerate wax ester lipid mixtures (roughly 60% and 40% composition by weight, respectively) are found in the melon and lower jaw fats across the family Delphinidae (Litchfield et al. 1975). These ratios differ substantially from blubber compositions. Slight variations of the delphinid lipid density and velocity mapping presented here should be sufficient for modeling the odontocete families Phocoenidae and Monodontidae. The families Platanistidae, Ziphiidae, and Physeteridae, however, may require different treatments.

Several aspects of Figure 10.2c merit mention. First, the attenuation range below -138 HU (below all soft tissue structures except air sacs) is again assigned the velocity of seawater (1,500 m/s). Next, soft tissue velocities above tendon (at 150 HU) and up to the bone threshold (at 300 HU) are modeled as a constant 1,730 m/s. This was done because the data range 150 to 300 HU corresponded to the range of partial-volume blurring of the soft tissue-bone interface, and because measured soft tissue velocities do not appear to exceed this value. The "partial-volume" effect is one of several potential sources of error in X-ray CT data (Cann 1988). It occurs when a scanned volume element straddles a sharp tissue interface, effectively blurring the interface. A large discontinuity in velocity at the bone threshold was introduced to correct for the artifact of partial-volume blurring of the soft tissue-bone interface. We also mention that partial-volume blurring of the skin-seawater interface was corrected using a simple technique (Aroyan 1996, p 91), but that no correction was made in the current model for tissue velocity dependence on temperature near the skin of the animal. Finally, note that the velocity above the bone threshold was modeled as a constant 3,450 m/s. The threshold for bone at 300 HU was determined by examining the thickness and continuity of skull surfaces crucial to acoustic behavior. As in previous two-dimensional simulations (Aroyan 1990; Aroyan et al. 1992), the 3-D results are not strongly dependent on the exact acoustical parameters assigned to bone.

Modeling of air spaces within soft tissue introduces unique difficulties. While the geometry of skull-soft tissue and external soft tissue-air interfaces is generally well represented in high-resolution X-ray CT data, air sacs inside soft tissues can suffer distortion due to postmortem changes. Modeling of a dolphin's nasal passages is further complicated by the common observation that the uppermost nasal sacs in live animals are, to some extent, mobile during phonation (Dormer 1979). Therefore, the author

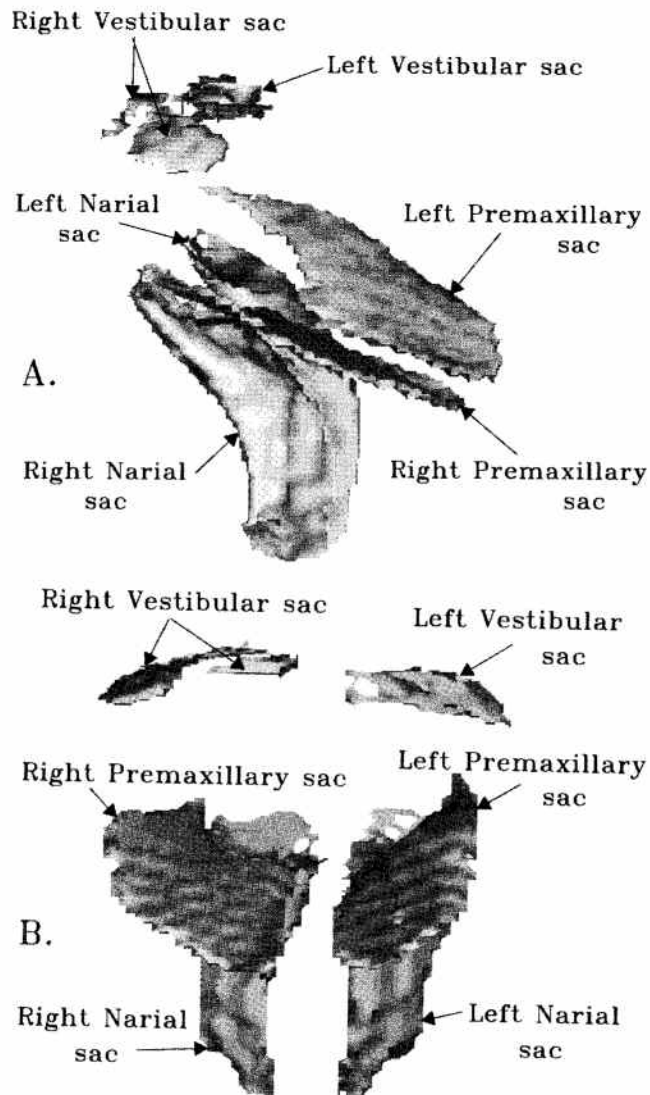


FIGURE 10.3. Visualizations of the model of the narial, vestibular, and premaxillary air sacs used in the simulations. Upper figure (A) is an elevated right-side view of the sac surfaces; lower figure (B) is an elevated front view. Labels identify the individual sacs included in the model.

chose the simplest model of the upper nasal sacs that was supported by the X-ray CT data and by previous anatomical studies.

Perspective views of this simplified air sac model are shown in Figure 10.3. Outlines of the narial air spaces were very clear in the *D. delphis* CT

data. The vestibular sacs, however, were only marginally discernable. By extracting all CT data coordinates with values below soft tissue thresholds, the nasal sacs and portions of the vestibular sacs were located. Unfortunately, the inferior vestibule, the spiracular cavity, and the premaxillary, nasofrontal, and accessory sacs were not even marginally discernible in this data. Nevertheless, the location of the premaxillary sacs is so well documented in the literature that the author deemed it permissible to include their positions above the premaxillary shelves of the skull in the model (Mead 1972; Dormer 1979). Note that portions of both left and right vestibular sacs, as well as other sacs in their entirety, are missing from this model.

As in previously reported simulations (Aroyan 1990; Aroyan et al. 1992), air sacs were simulated as pressure release surfaces by setting the pressure to zero at all sac coordinates. Note that this procedure eliminates any potential air-cavity resonance behavior.

3. Results of the Simulations

To provide an overview of the acoustical focal behavior of the head of the common dolphin, consider first the result of ensonifying a full head model with a (cw) 50-kHz sound beam incident from directly forward of the animal. Figure 10.4a illustrates the skin isosurface of this full model, which incorporated the skull, soft tissues, upper nasal air sacs, the peribullar sinuses surrounding most of the inner ears, and the pterygoid sinuses of the lower skull and palate. The full head model utilized the entire CT data set at half resolution (mapped to a 3.0-mm cubic grid). Figure 10.4b illustrates an isosurface at 30% of the maximum total acoustic energy density W_{total} (Eq. (2)) within the same model volume (and perspective) illustrated in Figure 10.4a. Significantly, three bright focal points occur within the model, each with an associated "funnel" or "channel" of energy density leading up to it. Funnels occur within both left and right fat bodies of the lower jaw, which narrow back to create sharp maxima against the lateral surfaces of each respective (left and right) tympanoperiotic complex. This channeling behavior of the lower jaw fat bodies strongly improves the forward receptivity of the simulated hearing patterns of both left and right ears (Aroyan 1996). The thinner-at-the-center thickness profile of each (left and right) lower jaw pan bone surrounded by low-speed fat apparently acts as a "fast" lens structure contributing to the creation of distinct forward receptivity peaks for each ear. The peribullar sinuses were also found to be highly effective in shielding the ears from directions of incidence other than forward and downward. All three results suggest mechanisms potentially fundamental to lower jaw hearing by delphinid cetaceans (Norris 1968, 1980); however, project results concerning the biosonar reception process must

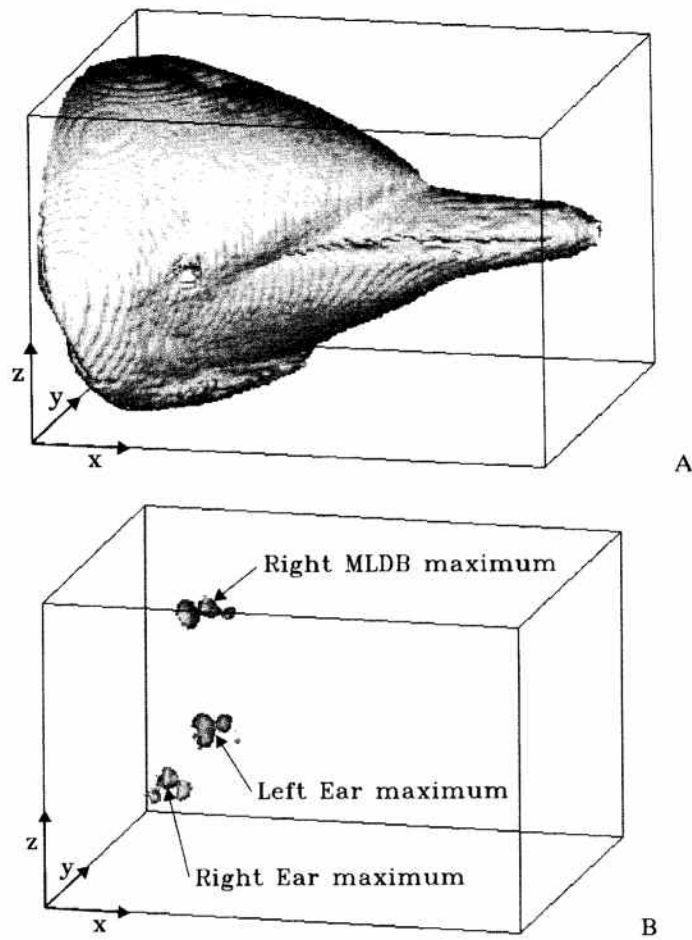


FIGURE 10.4. (A) Visualization of the skin isosurface of the full head model using the complete CT data set mapped to a 3.0-mm cubic grid. This rectangular model volume has x, y, z side-lengths of 44.7, 26.1 and 27.9 cm. (B) Illustration of an isosurface at 30% of the maximum total acoustic energy density W_{total} within the same tissue model volume (and perspective) illustrated in Figure 10.6 for a 50-kHz $(\theta, \phi) = (0^\circ, 0^\circ)$ inverse simulation (sound beam incident from straight ahead). The locations of the three bright focal maxima that occur within the model are labeled.

be discussed elsewhere. A funnel also occurs within the melon tissue of the forehead, which narrows back to create a bright maximum just below the right monkey lips-dorsal bursae (MLDB) complex (Cranford 1992; Cranford et al. 1996) within the soft tissue of the right nasal complex. This focal structure in the forehead and the locality of its maxima

recur over a range of ensonification directions for all frequencies tested and are quite robust with respect to biologically reasonable variation of the HU-to-density and HU-to-velocity model mappings discussed in Section 2.2.

We now proceed to examine in detail the focal behavior of the forehead tissues suggested by Figure 10.4b. Results of inverse and forward simulations are presented below for three different models of the forehead of the common dolphin: for a skull-only model, for a skull and soft tissues (including the melon) model, and for a complete skull, air sacs, and soft tissue model. We will also present the results of several moved source simulations using the complete model.

3.1 Skull-Only Simulations

The region of the CT data set selected for more detailed forehead simulations is illustrated by an isosurface at the CT data bone threshold (300 HU) in Figure 10.5a and by bone and skin isosurface in Figure 10.5b. This tissue region is a rectangular volume having x,y,z side-lengths of 27.0, 12.6, and 12.6 cm, represented on a 1.5-mm cubic grid. In the skull-only model, the HU-to-density and HU-to-velocity mappings of Section 2.2 were used to assign velocity and density values only to tissue coordinates with Hounsfield numbers equal to or greater than the bone threshold. All other model coordinates were mapped to background seawater density (1.03 g/cc) and velocity (1,500 m/s). The last few points of the density and velocity grids along the back, bottom, and side edges of the tissue region were graded back to seawater values in order to reduce spurious reflections at the model boundary.

The maxima of the inverse forehead simulations all occurred within a small volume of the supranarial region in all models. We will therefore illustrate the detailed inverse simulation data only within a subvolume of the forehead tissue model here referred to as the "potential source region" (PSR), which includes the supranarial region and extends forward to include about half of the melon body. The rectangular PSR volume (x,y,z side-lengths of 12.0, 9.0 and 9.0 cm) of the forehead model is outlined (boxed) in Figures 10.5a and b. To help establish positional reference with respect to the skull and soft tissue structures, Figure 10.5c illustrates a parasagittal slice through the center of the right MLDB complex within the PSR. Cranford et al. (1996) provide a review of relevant delphinid forehead tissue structures. The center of the left MLDB complex lies within the PSR, approximately 3.3 cm to the left and about 0.7 cm downward from the center of the right MLDB.

Figures 10.6a and b illustrate the acoustic potential energy density $W_{\text{potential}}$ in the PSR planes containing the maxima or "hypocenters" for skull-only inverse simulations at (cw) frequencies of 50 and 75 kHz, respectively. The direction of return propagation in this case was 5° below the

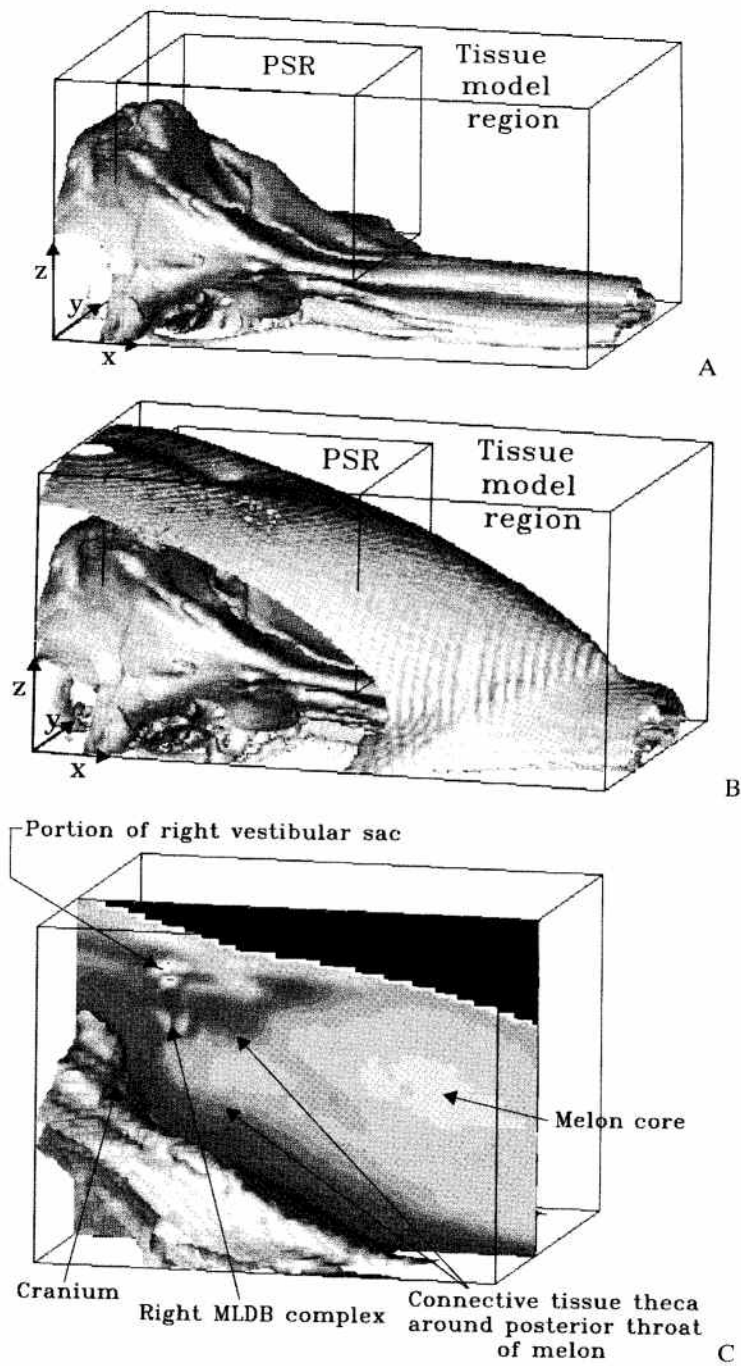


FIGURE 10.5. (A) Visualization of the outer skull isosurface within the region of the CT data set selected for the detailed forehead simulations. (B) Visualization of skin and bone isosurfaces within the same region of the CT data set. The potential acoustic energy density within the subvolume labeled "PSR" was visualized. (C) Perspective view of a parasagittal CT data slice through the center of the right MLDB complex in the PSR region. Several tissue structures are indicated and the skull isosurface added in order to provide positional reference in later diagrams of the results of the inverse simulations.

negative x-axis, which corresponds (via reciprocity) to a forward beam direction of 5° above the positive x-axis. Recall the logic of the inverse procedure: the maxima produced by a return beam will correspond to those positions within the tissue model that could, were sources placed there, best

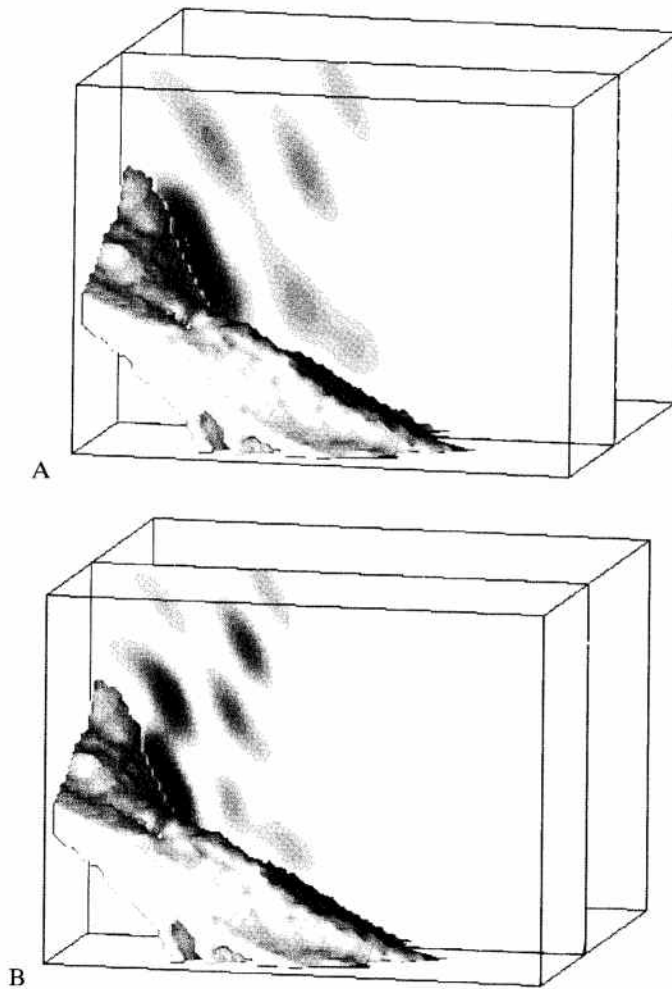
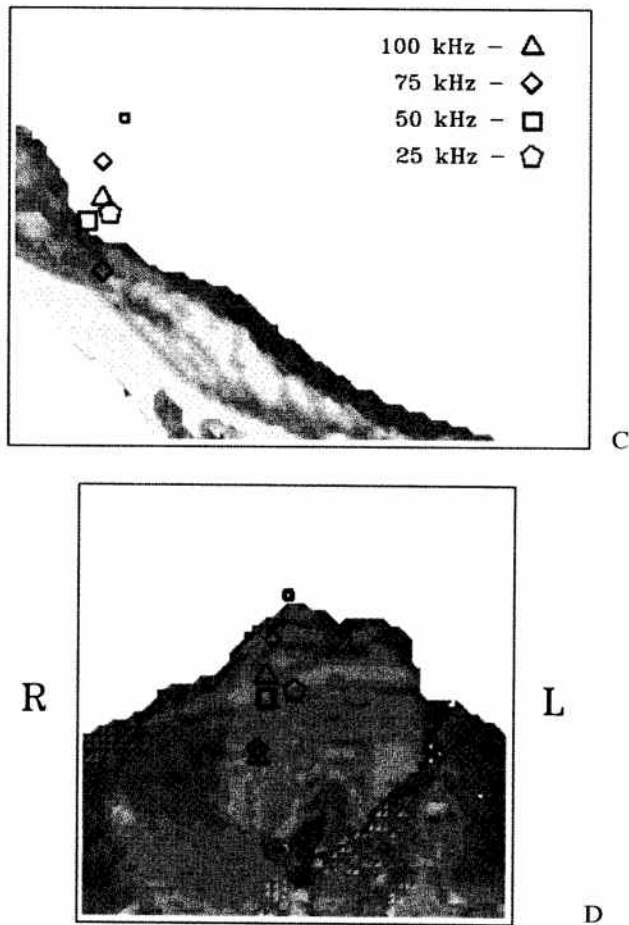


FIGURE 10.6. (A) and (B) Perspective illustrations of the potential energy density in parasagittal slices of the PSR containing the maxima for inverse $(\theta, \phi) = (5^\circ, 0^\circ)$ simulations with the skull-only model at frequencies of 50 kHz and 75 kHz, respectively. (C) and (D) Positions of the “hypocenters” from inverse $(\theta, \phi) = (5^\circ, 0^\circ)$ simulations with the skull-only model at four frequencies. (C) is a PSR view of the maxima positions from the right and (D) is a PSR view from the front. For multiple maxima, the size of the symbols is scaled to the energy of the maxima represented. The skull isosurface was added to all diagrams for positional orientation.

FIGURE 10.6. *Continued*

recreate a forward (emission) beam in the direction opposite the return beam. Focal tissue properties should be observable as a clustering of maxima over the relevant angles and frequencies. Because sonar beam angles are not well known for *D. delphis*, a limited range of vertical angles was tested for each tissue model in Aroyan (1996). In Figures 10.6a and b, patterns of spatial interference caused by reflections off of different portions of the skull surface are evident. Note that the positions of the maxima appear below the (right) MLDB and also up against the frontal bone. The maxima lying immediately against the skull may be caused in part by the process of reflection at hard surfaces, where the pressure amplitude nearly doubles, and the potential energy density almost quadruples. Indeed, the reader is cautioned against jumping to the conclusion that any one of these single frequency focal maxima is optimal for the animal—especially for the

simpler tissue models. As we shall see, multiple maxima appear in most of the models, although the ambiguity decreases significantly when the soft tissue density and velocity information and the air sacs are included. This is analogous to the situation in inverse seismologic simulations where ambiguity decreases with the accuracy and completeness of the geologic models assumed.

The positions of these ‘hypocenters’ for inverse simulations at the four frequencies, 25, 50, 75, and 100kHz, are shown in two PSR projections (viewed from the right and the front) in Figures 10.6c and d for the same direction of return propagation (an inverse $(\theta, \phi) = (5^\circ, 0^\circ)$ beam in the angular coordinate system of Figure 10.A1a in the Appendix). The maxima up against the skull is shown when it exists and also the “soft tissue” position (not against the skull) of highest potential energy density for each frequency. The general trends in the positioning of these skull-only focal maxima are clear. Along an anterior to posterior axis, foci only occur in the region of the upper narial depression, within a distance of about 3 cm (generally less) from the slope of the frontal bone. Along a transverse axis, they appear to fall along a line running up the right side of the narial depression, and not on the left. The two lowest foci appear to lie within the vertical range of the right nasal plug, while the main cluster lies roughly 1 cm behind and below the location of the right MLDB.

Consider now the emission patterns that result from placing point sources at the focal positions of the skull. Figure 10.7 illustrates the far-field emission distributions computed (using the forward simulation and extrapolation techniques discussed in Section 2.1 and Appendix A) for a point source with a frequency of 75 kHz placed at the $(\theta, \phi) = (5^\circ, 0^\circ)$ inverse simulation point of maximum potential energy density shown in Figures 10.6c and d (see Appendix A for explanation of the mapping of emission directions). Peak emission angles (in degrees) and the directivity indexes for these patterns are included in the figure. While a fair amount of energy is projected to the sides and upward, the skull by itself is capable of forming significant forward beams solely via reflection off of its upper surface for sources placed in the vicinity of the right narial depression. Emission simulations at 25, 50, and 100kHz also resulted in forward beams similar to Figure 10.7, with directivity indexes increasing approximately linearly with the logarithm of frequency.

3.2 Skull and Soft Tissue Simulations

For the skull and soft tissue model, the density and velocity of all points within the selected forehead region (see Figures 10.5a and b) were assigned by the mappings described in Section 2.2. Because these mappings assign all air CT scan voxels to the background seawater density (1.03 g/cc) and velocity (1,500 m/s) values, air sac regions were effectively “filled” with seawater in this model.

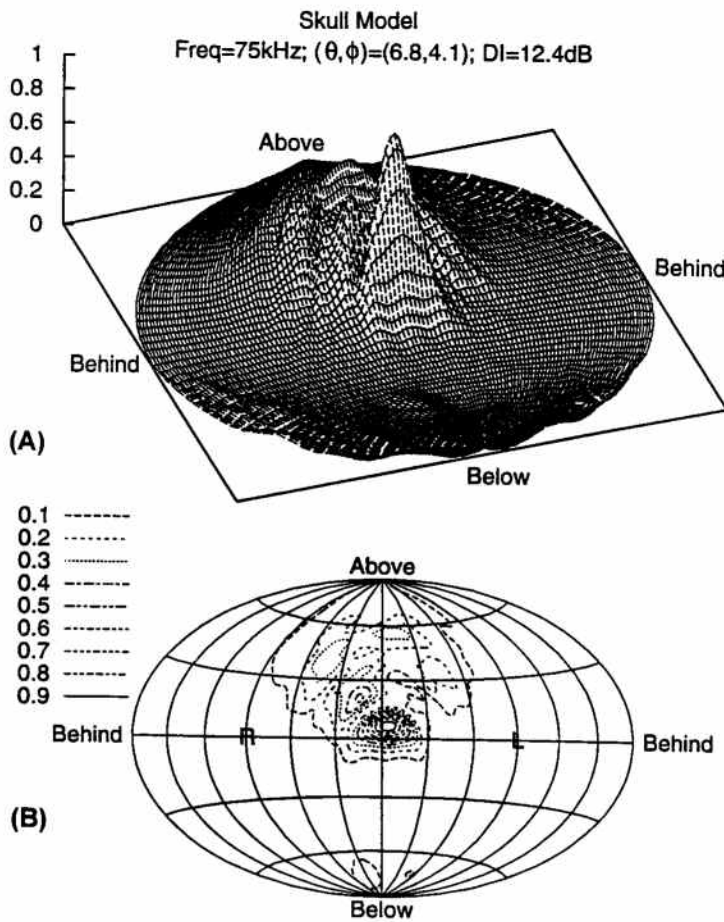


FIGURE 10.7. Extrapolated far-field emission pattern at 75 kHz for the skull-only model. The source point was the focal position of highest potential energy density obtained from a 75-kHz inverse $(\theta, \phi) = (5^\circ, 0^\circ)$ simulation. Diagram (A) plots intensity as height in a perspective view of the global far-field data. Diagram (B) is a contour plot of the same data projected downward into the plane of the global map. Direction angles (in degrees) of the emission peak and the directivity index for this pattern are indicated.

A surprising shift occurs in the patterns of acoustic energy flow through the PSR region when the soft tissues of the dolphin's forehead are added into the model. Figures 10.8a and b illustrate the potential energy density $W_{\text{potential}}$ in the parasagittal PSR slices that contained the soft tissue maxima from inverse $(\theta, \phi) = (5^\circ, 0^\circ)$ simulations with the skull and soft tissue model at frequencies of 50 and 75 kHz. The patterns no longer look simply like spatial interference caused by specular reflection from the hard skull

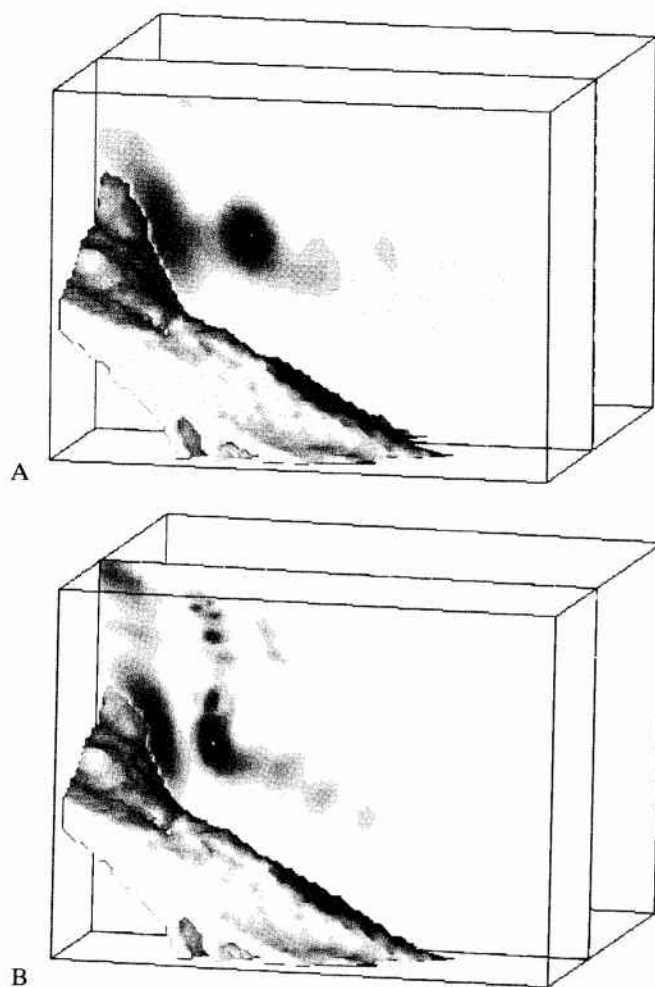
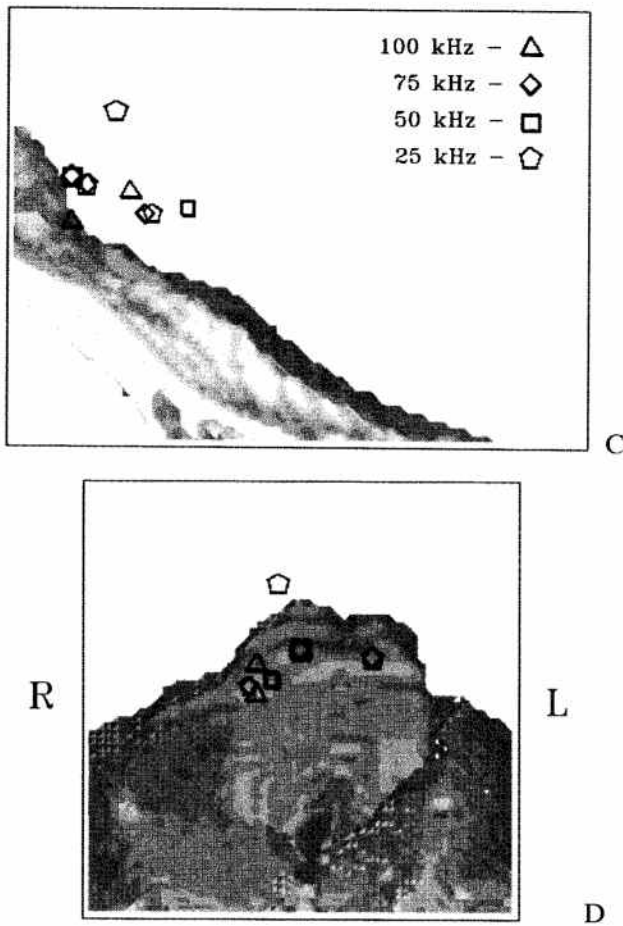


FIGURE 10.8. (A) and (B) Perspective illustrations of the potential energy density in parasagittal slices of the PSR containing the soft tissue maxima for inverse $(\theta, \phi) = (5^\circ, 0^\circ)$ simulations with the skull and soft tissue model at frequencies of 50 kHz and 75 kHz. (C) and (D) Positions of the “hypocenters” from inverse simulations with the skull and soft tissue model at four frequencies. (C) is a PSR view of the maxima positions from the right; (D) is a PSR view from the front. For multiple maxima, the size of the symbols is scaled to the energy of the maxima represented. The skull isosurface was added to all diagrams for positional orientation.

surface. A clear tendency toward collimation or channeling of energy is exhibited by the melon tissues. Energy is channeled in both vertical and horizontal sections back through a region passing approximately 1.0 cm ventral to the right MLDB complex. This channeling is most pronounced

FIGURE 10.8. *Continued*

within the posterior throat of the melon. The results at 25 and 100kHz (not pictured here) exhibit this same behavior.

Figures 10.8c and d shown the locations of the PSR focal maxima (viewed from the right and the front) from simulations at frequencies of 25, 50, 75, and 100kHz for an inverse $(\theta, \phi) = (5^\circ, 0^\circ)$ beam direction in the skull and soft tissue model. The maxima up against the skull is shown if it exists and the soft tissue position of highest potential energy density for each frequency. Again, note that the focal positions occur in the nasal passage region within a few centimeters of the cranial slope. Most appear on the right side, but two were located within 3mm of the cranial slope on the left side (left-sided maxima occurred in three instances with this model only). These left-sided maxima were positioned about 1.5cm posterior

to, and about 1.0cm medial to, the center of the left MLDB complex. Also, three maxima of the inverse $(\theta, \phi) = (10^\circ, 0^\circ)$ pattern (not pictured here) occurred against the skull down within the right nasal plug. Generally, however, the foci not lying against the skull appeared below the right MLDB.

The far-field emission pattern at 75 kHz for the skull and soft tissue model is illustrated in Figure 10.9. The distribution was computed for a point source at the 75-kHz inverse simulation foci of maximum potential energy density shown in Figures 10.8c and d. Note that addition of the soft tissues has narrowed the skull-only emission pattern. The melon (in combination with other soft tissues of the forehead) collimates much of the energy projected to the side and upward by the skull alone. The increased directivity index indicates a significant contribution by the melon to the formation of narrow biosonar beams.

3.3 Skull, Air Sacs, and Soft Tissue Simulations

The air sac model illustrated in Figure 10.3 was added to the skull and soft tissue model to form the skull, air sacs, and soft tissue model. This combined model constitutes a fairly complete representation of the dolphin's forehead tissues, although the air sac model was conservative (see Section 2.2). The results of this model are therefore of special interest.

Figures 10.10a and b illustrate the 10% isosurface level of the maximum PSR potential energy density $W_{\text{potential}}$ (viewed from above and from the right, respectively) for an inverse $(\theta, \phi) = (5^\circ, 0^\circ)$ skull, air sacs, and soft tissue simulation at 75 kHz. Energy collimation is clearly occurring in the melon, with strong channeling in both the vertical and horizontal directions back through a region passing approximately 0.7cm ventral to the right MLDB complex. Again, this channeling is most pronounced within the posterior throat of the melon. Note that the anterior melon also appears to be functioning as a lensing element (note the curvature of the anterior energy fronts in Figure 10.10a). Except for slightly sharper maxima, parasagittal PSR slices of the energy density in this model look very similar to the results pictured in Figure 10.8 for the skull and soft tissue model.

The focal maxima locations are plotted in Figures 10.10c and d (as viewed from the right and the front, respectively) for inverse $(\theta, \phi) = (5^\circ, 0^\circ)$ simulations at frequencies of 25, 50, 75, and 100kHz in the skull, air sacs, and soft tissue model. Again, the maxima up against the skull is shown when it exists and the soft tissue position of highest potential energy density for each frequency. Note that all of the foci occur on the right side of the nasal passages, not on the left, and that they have become fairly well grouped along the guide channel of the posterior melon, which passes roughly 0.7cm below the right MLDB. Besides the $\theta = 5^\circ$ maxima shown in Figure 10.14, focal positions were also determined for vertical return angles of 15° ,

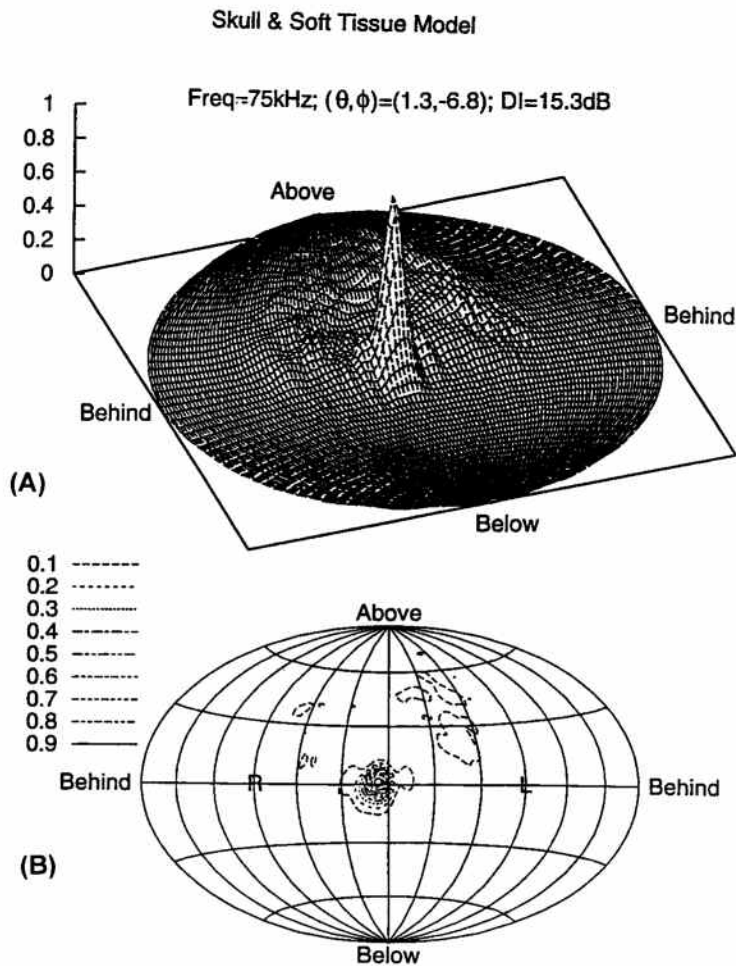


FIGURE 10.9. Extrapolated far-field emission pattern at 75 kHz for the skull and soft tissue model. The source point was the focal position of highest potential energy density obtained from a 75-kHz $(\theta, \phi) = (5^\circ, 0^\circ)$ inverse simulation. Diagram (A) plots intensity as height in a perspective view of the global far-field data. Diagram (B) is a contour plot of the same data projected downward into the plane of the global map. Direction angles (in degrees) of the emission peak and the directivity index for this pattern are indicated.

$10^\circ, 0^\circ, -5^\circ, -10^\circ,$ and -15° in the skull, air sacs, and soft tissue model. The focal positions appear well clustered throughout the $\theta = 5^\circ$ to -5° range of inverse results, and the average position of the cluster does not move appreciably.

Emission patterns, however, are most tightly focused for sources placed at the $\theta = 5^\circ$ inverse maxima of the skull, air sacs, and soft tissue model.

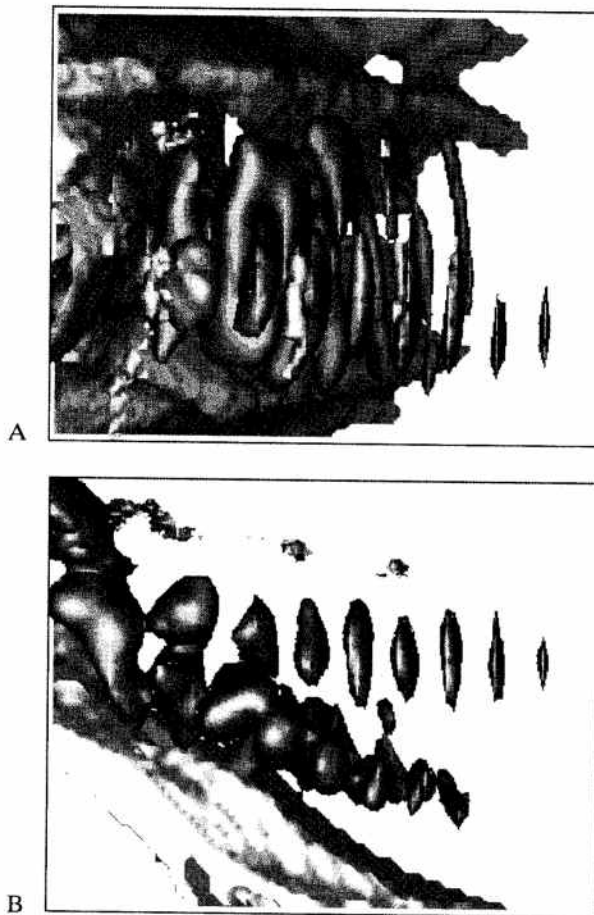
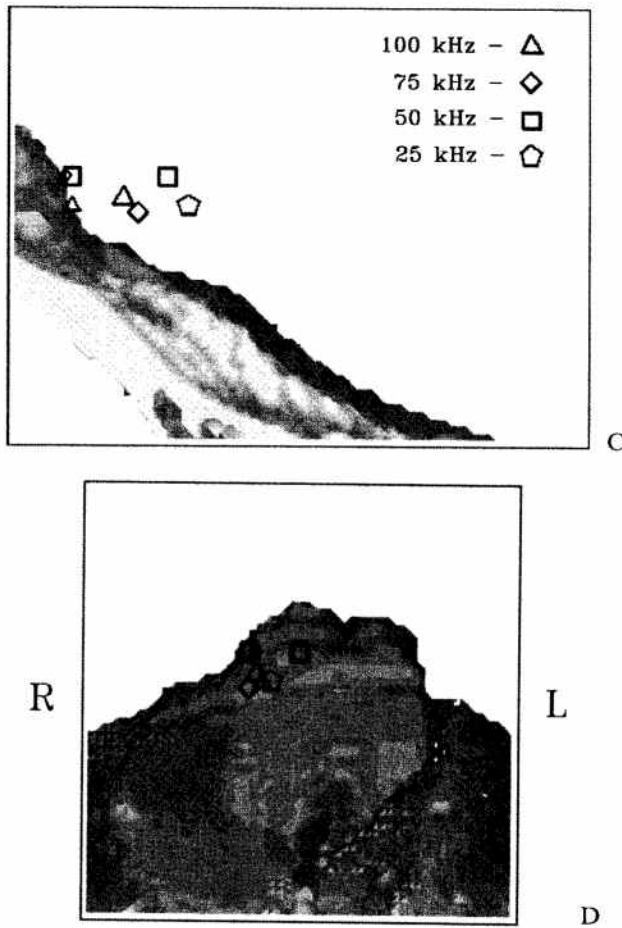


FIGURE 10.10. (A) and (B) Visualizations of the isosurface at 10% of the PSR potential acoustic energy density from a 75-kHz inverse $(\theta, \phi) = (5^\circ, 0^\circ)$ simulation with the skull, soft tissue, and air sacs model. (A) is a view of the PSR from above and (B) is a view of the PSR from the right. (C) and (D) Positions of the “hypocenters” from inverse $(\theta, \phi) = (5^\circ, 0^\circ)$ simulations with the skull, soft tissue, and air sacs model at four frequencies. (C) is a PSR view of the maxima positions from the right and (D) is a PSR view from the front. For multiple maxima, the size of the symbols is scaled to the energy of the maxima represented.

Figures 10.11 and 10.12 plot the far-field emission patterns that resulted from placing 25-, 50-, 75-, and 100-kHz point sources at the focal maxima of the inverse $(\theta, \phi) = (5^\circ, 0^\circ)$ simulations with this model. The complete forehead tissue model does indeed produce well-focused and relatively uniformly directed forward beams. Again, directivity indexes for these patterns increase approximately linearly with the logarithm of frequency. Incomplete diffraction rings are also noticeable at the lower frequencies.

FIGURE 10.10. *Continued*

3.4 Moved Source Simulations

Finally, we illustrate emission patterns for the complete skull, air sacs, and soft tissue model when the source point is moved to four locations previously conjectured to be the biosonar signal source location. Patterns were computed for 50- and 75-kHz point sources placed at the tip of the larynx, within the node of the right nasal plug, at the center of the left MLDB complex, and at the center of the right MLDB complex. The full head (half-resolution) model was used in the laryngeal source simulation; the truncated forehead (full-resolution) model was used in the other three moved source simulations.

Figure 10.13 illustrates the 75-kHz far-field pattern contours for these four conjectured source locations. Note that the laryngeal source location

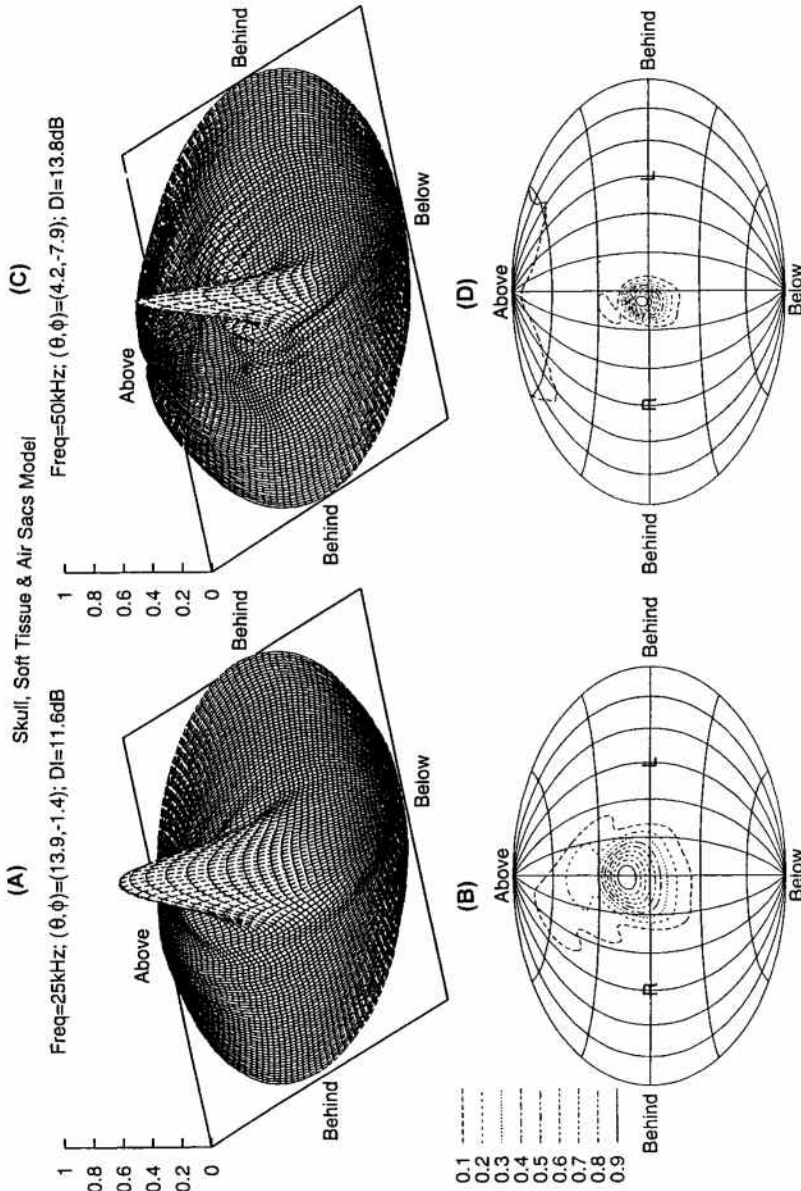


FIGURE 10.11. Extrapolated far-field emission pattern at 25 and 50kHz for the skull, soft tissue, and air sacs model. The source points were the focal positions of highest potential energy density obtained from inverse $(\theta, \phi) = (5^\circ, 0^\circ)$ simulations.

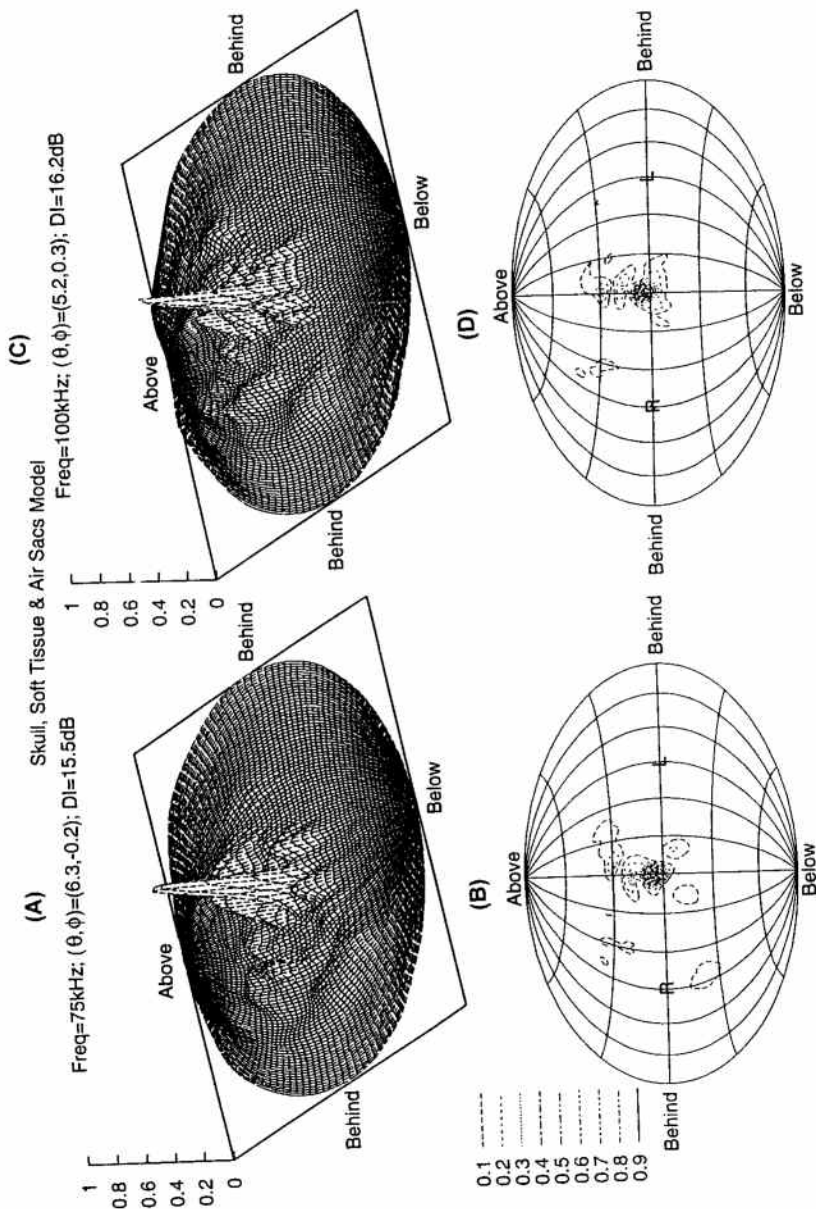


FIGURE 10.12. Extrapolated far-field emission pattern at 75 and 100kHz for the skull, soft tissue, and air sacs model. The source points were the focal positions of highest potential energy density obtained from inverse $(\theta, \phi) = (5^\circ, 0^\circ)$ simulations.

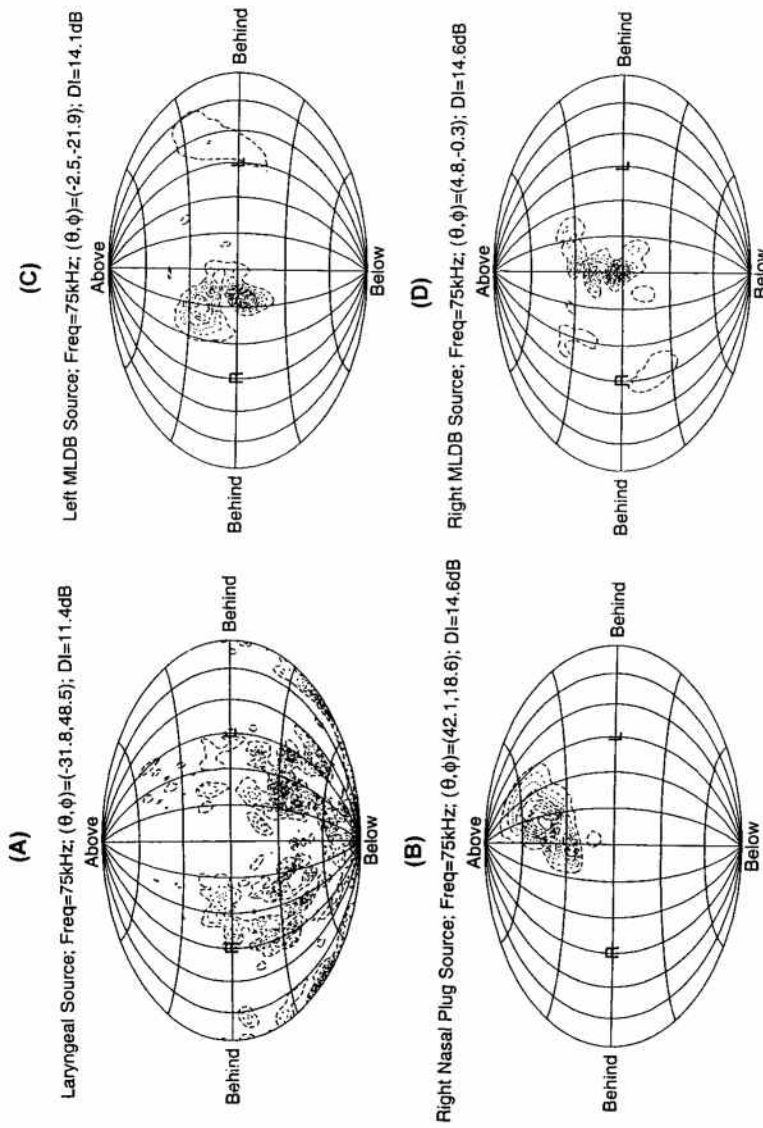


FIGURE 10.13. Contour plots of extrapolated far-field emission patterns for a 75-kHz point source placed at various tissue locations. (A) Placed at the tip of the larynx in the full head model. (B) Placed within the right nasal plug node in the complete forehead model. (C) Placed at the center of the left MLDB complex in the complete forehead model. (D) Placed at the center of the right MLDB complex in the complete forehead model.

mainly produces scattered downward and sideways emissions. Sources placed in the right nasal plug node projected sound forward at rather high vertical angles (average $\theta = 38^\circ$) and somewhat left of forward. The left MLDB source location projected beams averaging about 26° right of forward. The right MLDB source location produced approximately centered beams with some secondary lobe energy into higher vertical angles.

4. Discussion of Results

As with all bioacoustic tissue simulations, the results of this study are dependent on both the accuracy of the wave propagation techniques and on the fidelity of the tissue models to *in vivo* tissue geometry and acoustic properties. Although shear wave modes were ignored, the accuracy of the compressional wave propagation techniques was demonstrated in Aroyan (1996) to be excellent. Tissue geometry is generally well represented in high-resolution X-ray CT data, but some displacement of the supranarial soft tissues may have occurred through air sac collapse. However, the scan methodology of Cranford (1992) was developed to minimize gross post-mortum tissue distortion. While approximate, the technique used to model the acoustic properties of soft tissues is based on established tissue mass density scan practices and on the measured acoustic properties of mammalian and unique delphinid tissues. In addition, simulation results were found to be quite robust with respect to biologically reasonable variation of the HU-to-density and HU-to-velocity model mappings. This may in part be due to the relatively short tissue propagation paths (generally less than 10 wavelengths) involved in the simulated emission processes. While many opportunities exist to refine the analysis, the work presented here is sufficient to reach a number of interesting conclusions.

The role of the skull in acoustic beam formation has been investigated using both acoustic sources and ray tracing techniques (Evans et al. 1964), using lightbulb-as-source techniques (Dubrovskiy and Zaslavskiy 1975), using acoustic sources with and without soft tissue present (Romanenko 1973), and using two-dimensional bioacoustic simulations (Aroyan 1990; Aroyan et al. 1992). The results of the three-dimensional skull-only forehead simulations have corroborated and extended the conclusions of these previous studies. The common dolphin's skull plays a predominant role in beam formation by establishing the basic focal geometry of the forehead. The skull by itself is capable of forming significant forward beams solely by reflection off of its upper surfaces. Focal maxima were found only in the immediate vicinity of the asymmetrically enlarged right narial depression, and not elsewhere. The fact that these maxima occurred only on the right side of this depression and not on the left suggests that the focal geometry of the skull is functionally related to its asymmetry. Because air sacs cover portions of the skull surface in the vicinity of the nasal passages, the focal

geometry demonstrated here apparently also shapes and supports the highly reflective flesh-air sac boundaries. In the common dolphin, skull acoustic asymmetry parallels the asymmetry of the refractive soft tissues of the forehead, as discussed below.

Much speculation has surrounded the acoustic role of the fatty melon tissues of the delphinid forehead. Wood (1964) suggested that the melon may both focus and acoustically couple internally generated sound to seawater. Sound speed measurements on the melon of a Pacific bottlenose dolphin (Norris and Harvey 1974) revealed a low-velocity core and a graded outer shell of high-velocity tissue. A number of biomolecular studies have confirmed that the lipids of the delphinid melon are chemically distinct from other body fats and blubber. Evans et al. (1964) found that the presence of the soft tissue of the bottlenose dolphin's forehead caused narrower beams to be emitted than were produced by the skull alone. Romanenko (1974) measured horizontal beam widths with the whole head that were roughly half as wide as the widths obtained using the skull alone for frequencies of 80 kHz and higher. Previous two dimensional simulations (Aroyan 1990; Aroyan et al. 1992) suggested that a melon velocity profile of the magnitude measured by Norris and Harvey (1974) is capable of mild focusing.

The current project substantiates the results of these earlier investigations of the acoustic function of the delphinid melon. The 3D skull and soft tissue simulations have demonstrated that the melon and other soft tissues of the *D. delphis* forehead significantly narrow the main forward beam, corroborating the results of Evans et al. (1964) and Romanenko (1974), and confirming the conjectures of Wood (1964) and Norris (1968). The melon's efficiency in narrowing the horizontal beam width generally appears greater than its effect on the vertical width. In addition, the inverse skull and soft tissue simulations demonstrated a pronounced tendency towards collimation or channeling of acoustic energy within the posterior throat of the melon. The posterior throat of the melon appears effective as a partial wave-guide, while the larger forward lobe of the melon has been confirmed to operate as a lens in the acoustic emission process.* Perhaps the magnitude of these effects explains the extraordinary metabolic investment that the specialized melon tissues represent in the evolution of odontocete cetaceans, as suggested by Morris (1986).

* See the discussion of fundamental acoustic mechanisms in Aroyan (1996, pp. 28-34). A three-component model of the delphinid biosonar emission system is proposed consisting of an impulsive source mechanism (the MLDB source hypothesis of Cranford et al. 1987), a damped resonant chamber surrounding this source (formed by the partially air-bounded soft tissue of the delphinid nasal passages), and a projector of the ensuing signal consisting of the skull, the melon and other soft tissues of the forehead. Simplified calculations with this model correctly predict the frequency ranges and modal/bimodal signal structures of several odontocetes as a function of signal source level and body size. The surprising consequences of this simple model will be discussed in later reports.

To illustrate the physical basis of melon focal behavior, Aroyan (1996) plotted the density, velocity, and impedance structure in a two-dimensional slice through the *D. delphis* melon and forehead using the modeling techniques of Section 2.2. These plots reveal an impedance matched melon-sea-water interface, confirming the matched impedance hypothesis of Wood (1964). They also reveal a broad velocity depression in the anterior melon that narrows posteriorly to form a well defined channel through the rear throat of the melon. The broad velocity depression is indicative of a lensatic function for the anterior melon, as conjectured by Wood (1964) and proposed in greater detail by Norris (1968). The posterior velocity channel appears analogous to a flared wave-guide. The velocity of the melon "wall" rises somewhat gradually to a maximum of about 20% above the velocity of the channel in the posterior melon. While a velocity reduction of 20% within a waveguide of uniform geometry may permit highly efficient guiding of specific wavefunctions, the short and widely flared throat of the posterior melon in this dolphin is probably best characterized as a partial or "leaky" wave-guide of biosonar clicks.

An incomplete model of the nasal air sacs has been shown to improve the forward reflection of energy projected upward, sideways, and downward by the skull and soft tissue model. Addition of the air sacs into the model always raised the directivity indexes of the patterns, although the importance of this contribution varied with frequency. Generally speaking, the air sac model was effective in forward collimation of energy projected upward, sideways, and downward by the skull along, while the melon was effective in narrowing (focusing) the main forward lobe. Both the air sac model and the melon, however, contributed to both effects. Nevertheless, a precise evaluation of the relative contribution of the nasal air sac system to beam formation must await better information on the exact configuration of the air sacs during click production.

The biosonar signal source tissues in the common dolphin were found to be localized within a remarkably small volume of the nasal passages. A dramatic clustering of inverse simulation foci for all frequencies tested in the complete model implicates approximately 1 cc of tissue centered about 0.7 cm below the center of the right MLDB complex as the most plausible "hypocenter" of the dolphin's biosonar clicks. However, the posterior lip of the MLDB complex is often displaced dorsally with respect to the anterior lip in postmortem specimens (Cranford et al. 1996). It is possible that some or all of the soft tissues of the supranarial region were displaced slightly from their air-metering configuration during biosonar click production. In the author's opinion, the clustering of focal points best supports the conjecture that the *right* MLDB complex is the source tissue of the pulsed biosonar signals of this dolphin. Inverse simulation foci were notably absent from other previously proposed source locations including the left MLDB, the larynx, and the right nasal plug node. In the complete model, foci were found only on the right side of the nasal passageway and not on the left. The nonviability of the larynx and right nasal plug as source locations for

biosonar clicks was further illustrated by forward extrapolations of the far-field patterns produced by point sources placed at the tip of the larynx and within the node of the right nasal plug in the complete model.

A surprising degree of acoustic asymmetry was also discovered. In the *D. delphis* specimen, forehead asymmetry is developed to a point where very different beams are produced by left and right MLDB sources. The centers of the left and right MLDB complexes are separated by about 3.4 cm in this specimen. Sources placed just below the right MLDB complex produced well-focused forward-directed beams, while sources placed at the left MLDB produced somewhat scattered emission patterns peaked roughly 26° to the right of center forward. These differences have a significant bearing on the conjecture that both complexes may be used simultaneously to produce coherently interfering beams (Cranford et al. 1996). Dual MLDB source simulations above 50 kHz (not illustrated here) have shown that coherent forward beaming is constrained by the well separated pattern peaks. Even if dual MLDB source coordination on a time scale of microseconds were biologically possible, phasing would have little effect on the resulting multi-lobed emissions.

Perhaps the central conclusion of the current investigation was that the forehead tissues of the *D. delphis* model exhibit a simple focal structure for forward-directed beams, with the right MLDB (or slightly below) as focal center. While the behavioral evidence generally does not support the occurrence of multi-lobed emission patterns in delphinids (Dormer 1979; Mackay and Liaw 1981; Au 1993), it is possible that previous experiments have not been designed to encourage this behavior. Some dolphins appear capable of selectively producing sonar pulses at either the left or right MLDB (Cranford, Chapter 3). Nevertheless, it remains probable that the asymmetrically enlarged tissues of the right side are indeed specialized for click production (Mead 1975). As suggested by Heyning (1989), "there may have been selection for a single sound generating source in the narial region in order to avoid interference generated from two sound sources." The development of separate motor control would also have contributed to the avoidance of sonar beaming problems.

The overall beam forming capability of the forehead tissues demonstrated here for the common dolphin is impressive. We have seen that the complete forehead tissue model produces relatively uniformly directed and well focused forward beams when appropriate source locations are used. The -3 dB beam widths of approximately 12° (vertical) and 11° (horizontal) in the 100 kHz pattern are consistent with the experimentally measured broadband (peaked near 120 kHz) beam widths of 10.2° (vertical) and 9.7° (horizontal) for *Tursiops truncatus* (Au et al. 1978). The directivity indexes computed here for the complete *D. delphis* model, however, fall roughly 10 dB below those reported for *T. truncatus* (Au et al. 1978; Au 1980). Taking both frequency and size differences into account for these animals, a disparity of roughly 5 dB remains. In this context, it is important to note that

two peculiarities of the model may have contributed to lowering the computed directivity indexes. First, the incomplete air sac model may have lowered the computed indexes at all frequencies. Second, because point sources emit uniformly in all directions, one expects the use of point sources in these simulations to have lowered the computed directivity indexes by amounts that depend on the frequency and assumed geometry of the signal generator. For these reasons, the demonstrated focal characteristics of the forehead tissues are expected to be conservative.

The forehead tissue structures of the common dolphin are representative of members of the odontocete family Delphinidae having an intermediate-to-moderate value of soft tissue asymmetry (Cranford 1992). It is expected that similar if not identical mechanisms operate in all delphinids exhibiting intermediate-to-moderate soft tissue asymmetry (including *T. truncatus*). It is also reasonable to suggest that similar mechanisms may operate in all odontocetes that possess forehead tissue morphologies resembling those of the common dolphin.

The techniques utilized here to investigate the biosonar system of *D. delphis* are applicable to many other marine mammal species. Investigation of odontocete species with better studied biosonar emission fields (i.e., *T. truncatus*, *Delphinapterus leucus*, *Pseudorca crasidens*) would serve to test the generality of the emission mechanisms discussed above. In addition to sound emission, the same techniques may be used to model hearing. Aroyan (1996) simulated individual right and left ear receptivity patterns and tissue reception pathways in the common dolphin using techniques that are widely applicable to other marine mammals. Extensions of the method for modeling the acoustical parameters of biological tissues from X-ray CT data presented in Section 2.2 may enable a host of bioacoustic applications. Finally, the power of combined propagation and extrapolation techniques has yet to be exploited in several areas of physical acoustics.

5. On the Physics of Sound Production in the Blue Whale

Blue whales (*B. musculus*) produce loud low-frequency underwater sounds, providing a practical tool to study whale distribution and movements (Thompson and Friedl 1982; McDonald et al. 1995; Stafford 1995). The blue whale is not only the largest animal alive, but is also the loudest, making it an excellent choice for sound production mechanism study. Previous publications on the physics of the baleen whale sound production mechanism have concentrated on bubble resonance (Harris 1964; Barham 1973), a phenomena where a given air volume at a given depth will resonate to produce sound efficiently at an acoustic frequency that can be calculated. We propose that a Helmholtz resonance better fits the observations in that, unlike bubble resonance, Helmholtz resonance provides efficient

constant frequency sound production over changing depths, allowing the whale improved efficiency in monotonic sound production. Previous studies have provided anatomical information and speculation on how baleen whales may produce sound (Hosokawa 1950; Yablokov et al. 1972; Sukhovskaya and Yablokov 1979; Purves and Pilleri 1983; Quayle 1991; Reidenberg and Laitman 1992, 1993; Haldiman and Tarpley 1993). Our goal is to integrate the physics of sound production with blue whale laryngeal anatomy to develop a verifiable model of how the blue whale produces sound.

Before applying physical constraints to sound production in blue whales, it is helpful to understand the variability within the blue whale call repertoire. Calls from the blue whales observed off the California shore have been the most studied, and can be divided into four fundamental types, shown in Figure 10.14: (A) typically the first call of a series, consisting of about 20 pulses spaced about 0.8 s apart, with each pulse subdivided into multiple, time-offset nonharmonic components; (B) a harmonic sound typically 19 s in duration, sweeping or stepping down slightly in frequency from about 20 Hz to 16 Hz; (C) a 9- to 12-Hz upswept tone preceding a type B call; (D) an 80- to 30-Hz downsweep typically 2 to 5 s in duration, often produced by multiple animals as counter-calls and not produced in combination with the other call types. It is only the type B calls that provide a unique constraint on the sound production model. Only the type B call is of continuous long duration such that the sound production mechanism is unlikely to be able to recirculate the air used in producing the call. The calls shown in Figure 10.14a were recorded in the Santa Barbara Channel using sonobuoy arrays for localizing the sound source in combination with visual localization, leaving little doubt that blue whales were the source of these sounds. Similar calls have been recorded from blue whales off California, Oregon, and Baja California, Mexico (Thompson et al. 1992; D'Spain et al. 1995; McDonald et al. 1995; Stafford 1995; Rivers 1997). Type B calls have reported source levels up to 190 dB re 1 μ Pa in recordings made off San Nicolas Island, California (Aburto et al. 1997). The duration of the type B calls illustrated in Figure 10.14 ranges from 16 to 21 s. The type A and B blue whale calls often occur in patterns with regular pauses between calls and longer pauses during breathing periods (Cummings and Thompson 1971; McDonald et al. 1995; Stafford 1995).

Blue whales have geographic call character variation, the animals off the west coast of North America having similar call character for more than thirty years (Thompson 1965) while blue whale calls from other regions are distinctly different (Weston and Black 1965; Kibblewhite et al. 1967; Cummings and Thompson 1971; Northrup et al. 1971; Thompson and Friedl 1982; Alling and Payne 1988; Alling et al. 1991) suggesting learned call character within geographic variations as occurs in birdsong (Kroodsma 1996). The type B call off the west coast of North America provides the longest continuous sound from blue whales known to the authors.

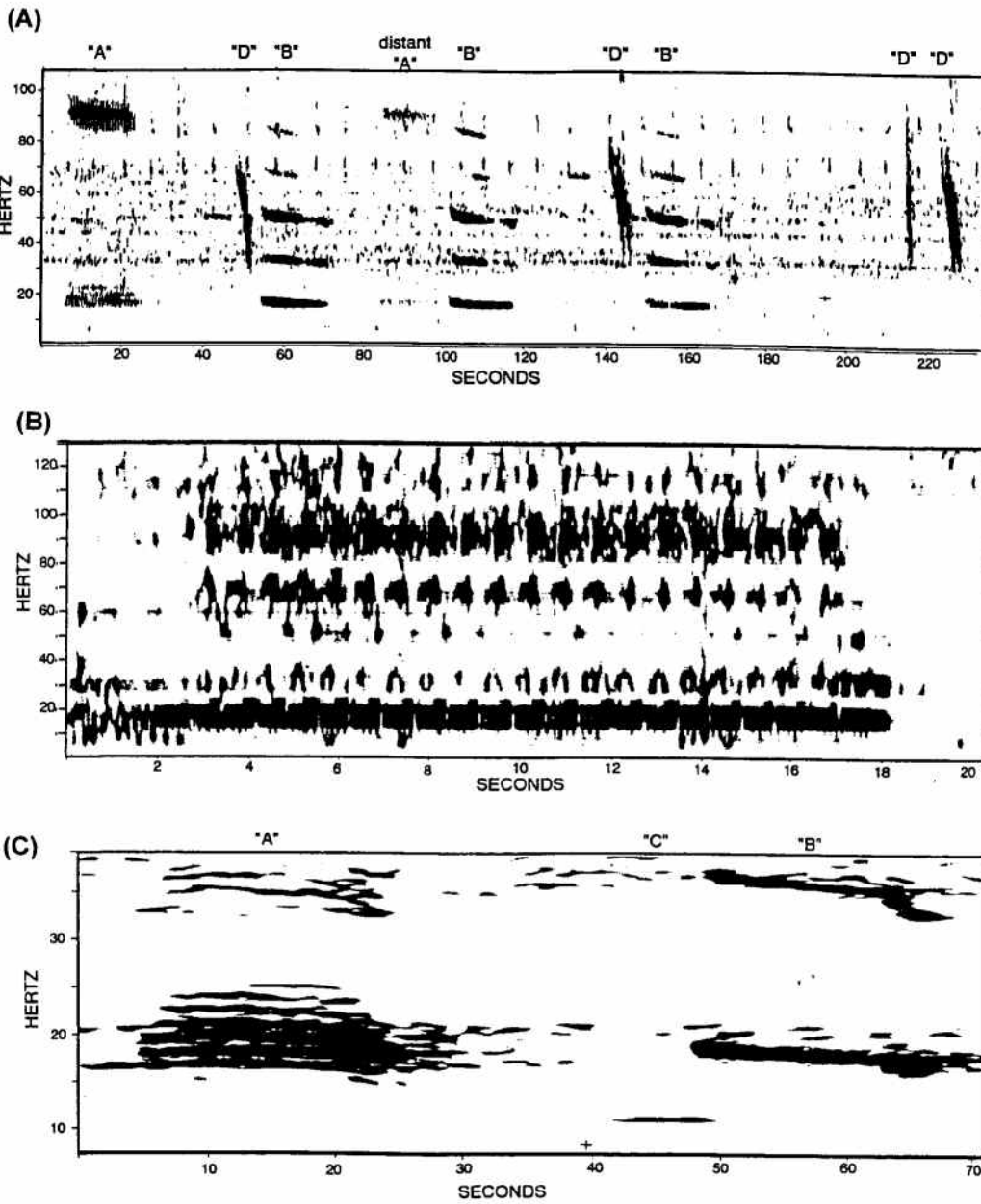


FIGURE 10.14. Examples of the four most common blue whale call types (A–D) recorded off the west coast of North America are shown as spectrograms. (A) Sequence of type “A” and “B” calls recorded on a sonobuoy array in the Santa Barbara channel, California, the loudest “A”–“B” series is believed to be produced by a single animal, interspersed with some short downsweep “D” calls produced by a second animal. Weaker calls can be seen in the background from another animal. The spectrogram was computed with 1 s FFT length, 97% overlap, and a Hanning window. Frequency response is boosted 1.5 dB/octave above 10 Hz. See text for details on parts B and C.

6. Blue Whale Sound Production Model

6.1 *Water, Solid, or Air*

All possible mechanisms for sound production in the blue whale must involve radiating sound into seawater, but the oscillating media could, theoretically, be made of water, bone, or air within the whale. Sound can be produced underwater by fluctuations in water pressure (water), as in a hydrodynamic oscillator (Albers 1965, pp. 176–177); by vibration of rigid materials (solid), as in the sounds produced by snapping shrimp (Albers 1965, pp. 221–227) and possibly the jaws of whales (Brodie 1993); or by oscillations of an air-filled chamber (air), as is the case in most biological sound production systems. A water-filled source may be possible in a whale using a hydrodynamic oscillator based on the large water-filled pleated ventral cavity of a blue whale, perhaps using the flexible walls as a waveguide to shorten the dimensions required to achieve resonance at 17 Hz (Fletcher 1992). Such a water-based sound source would appear to be very inefficient due to losses associated with moving the whale's ventral tissues. Another possibility is to design a resonant 17-Hz oscillator based on shear mode vibrations of the lower jaw bone of a blue whale, but again this would be an inefficient sound radiator, the bone dimensions being significantly less than the 22-m optimum length for an efficient dipole radiator. Systems able to compress water or bone are considered less efficient than air-filled systems and require much higher differential pressures. The system that is the least complex, most versatile, and most efficient is an air-filled cavity oscillation.

6.2 *Volume Displacement Requirements*

Just as a human singer can hold a note only until all the air in the lungs is expired, we believe the blue whale can only produce a continuous call of given intensity and frequency for some maximum duration dependent on the volume of air available. We assume the whale has no system equivalent to a series of pumps and valves that would allow continuous recirculation of air. The volume of air required to produce an underwater sound is then dependent on the displacement required to produce each cycle of a sound of given intensity, given frequency, and the resonance of the system, which is a direct measure of the efficiency of producing that displacement. The resonance quality factor is proportional to the efficiency and is discussed later, but first we calculate the displacement requirements.

The intensity of an underwater sound produced by oscillation of an air-filled cavity can be directly related to the associated volume displacement required to produce each cycle of that sound. The whale is compact in an acoustical sense, so that the displacement is the total net fluctuation in the volume of the whale each cycle, requiring air to be alternately compressed and released. Assuming this compression occurs as air is moved past a fluc-

